Rapid Growth of TiO$_2$ Nanoflowers via Low-Temperature Solution Process: Photovoltaic and Sensing Applications

M. Shaheer Akhtar [1,*], Ahmad Umar [2,*], Swati Sood [3], InSung Jung [1], H. H. Hegazy [4,5] and H. Algarni [4]

[1] New and Renewable Energy Material Development Center (NewREC), Chonbuk National University, Chonbuk 54896, Korea; kjunggye@jbnu.ac.kr

[2] Department of Chemistry, Faculty of Science and Arts and Promising Centre for Sensors and Electronic Devices (PCSED), Najran University, Najran 11001, Saudi Arabia

[3] Department of Chemistry and Centre of Advanced Studies in Chemistry, Panjab University, Chandigarh 160014, India; swati17sood@gmail.com

[4] Department of Physics, Faculty of Science, King Khalid University; P.O. Box 9004, Abha 61421, Saudi Arabia; hosam_h_hegazy@yahoo.com (H.H.H.); halgarni@hotmail.com (H.A.)

[5] Department of Physics, Faculty of Science, Al-Azhar University; Assiut 71524, Egypt

[*] Correspondence: ahmadumar786@gmail.com (A.U.); shaheerakhtar@jbnu.ac.kr (M.S.A.)

check for updates

Abstract: This paper reports the rapid synthesis, characterization, and photovoltaic and sensing applications of TiO$_2$ nanoflowers prepared by a facile low-temperature solution process. The morphological characterizations clearly reveal the high-density growth of a three-dimensional flower-shaped structure composed of small petal-like rods. The detailed properties confirmed that the synthesized nanoflowers exhibited high crystallinity with anatase phase and possessed an energy bandgap of 3.2 eV. The synthesized TiO$_2$ nanoflowers were utilized as photo-anode and electron-mediating materials to fabricate dye-sensitized solar cell (DSSC) and liquid nitroaniline sensor applications. The fabricated DSSC demonstrated a moderate conversion efficiency of ~3.64% with a maximum incident photon to current efficiency (IPCE) of ~41% at 540 nm. The fabricated liquid nitroaniline sensor demonstrated a good sensitivity of ~268.9 μA mM^{-1} cm^{-2} with a low detection limit of 1.05 mM in a short response time of 10 s.

Keywords: TiO$_2$ nanoflowers; photovoltaic device; chemical sensor; nitroaniline; sensitivity

1. Introduction

Recently, metal oxide nanomaterials like titanium oxide (TiO$_2$), zinc oxide (ZnO), nickel oxide (NiO), tin oxide (SnO$_2$), cobalt oxide (Co$_3$O$_4$), iron oxide (Fe$_2$O$_3$), etc. have been regarded as some of the most important multi-functional materials because of their excellent functionalities and applications, such as electrochemical, photocatalytic, photo electrochemical, electronics, sensing, and so on [1–5]. Among various metal oxides, TiO$_2$ nanostructures possess a special place because of their excellent properties, such as a wide band gap, low toxicity, easy synthesis, good stability, etc., and efficient applications in lithium ion batteries, solar cells, chemo-sensors, photocatalysts, and so on [5–9]. TiO$_2$ nanostructures including nanotubes [10], nanoflakes [11], nanorods [12], solid and hollow spheres [13], and urchin-like [14] hierarchical TiO$_2$ structures, have already been fabricated through a variety of solution techniques. In particular, the TiO$_2$ nanostructures with 1D and 2D dimensions like nanorods, flowers, urchins, etc. often express additional extraordinary chemical/physical properties such as improved surface-to-volume ratio, fewer structural defects, and a large interspace [15,16].

M. Ghosh et al. reported on the fabrication of "nanorods-on-nanofiber" heterostructures by the distribution of V_2O_5 nanorods on TiO_2 nanofibers via the gas jet fiber (GJF) spinning process, and these heterostructures showed excellent photocatalytic activity due to the slowdown of the electron–hole charge recombination phenomena [17]. H. Liu et al. recently studied the direct synthesis of TiO_2 crystals with flower-like structures by a facile hydrothermal method using tetrabutyl titanate (TBT) as a titanium source and ethylene glycol as an additive [18]. They found that TiO_2 crystals with flower-like structures exhibited high photocatalytic activity for the degradation of methylene blue (MB) under UV-vis light irradiation because these nanostructures had a considerably high surface area. Thus, it can be assumed that nanostructures with a flower-like structure might favor the achievement of high specific surface area and the enlargement of active sites.

TiO_2 is considered to be a pioneering material for dye-sensitized solar cells (DSSCs), which are photovoltaic devices that convert light energy to electrical energy through a semiconductor junction. Recently, the DSSC has become known as an emerging photovoltaic (PV) device owing to its low cost, simple manufacturing, and high solar-to-electrical conversion efficiency [19–22]. As a result, DSSCs are gaining wide research interests among the scientific community. Nanostructured TiO_2 films have been used to fabricate DSSCs with light-to-electricity conversion efficiency (η) of 1.9% [23]. Using exposed mirror-like plane {001} facets of anatase TiO_2, Zhang et al. fabricated efficient DSSCs as such mirror like facets exhibited light-reflecting ability, which led to better light to electricity conversion efficiencies [24]. Recently, Yang et al. fabricated hierarchical hollow microspheres of a TiO_2-based DSSCs which possessed high conversion efficiency due to the specific and novel morphologies of the TiO_2 material [25]. Thus, to obtain better photovoltaic performances, it is important to examine the various specific morphologies of TiO_2. Herein, we report the photovoltaic performance of anatase-phase synthesized TiO_2 nanoflowers by a facile low-temperature solution process.

Along with photo-efficient energy conversion, metal oxides also find great applications in the sensing harmful and toxic gases, chemicals, or biomolecules. There is a great need for the efficient and sensitive detection of chemicals which are hazardous even in minimal concentrations, (e.g., toxic organic compounds like aliphatic and aromatic hydrocarbons, especially phenols, nitrophenols, nitroanilines, etc.). Recent studies have demonstrated that metal oxide nanomaterials can be used as efficient and sensitive chemo-sensors for volatile organic compounds (VOCs) such as ethanol, methanol, propanol, acetone, methylene chloride, benzene, butanol, xylene, isopropanol, and so on [26–32]. Among aromatic compounds, nitroaniline is considered a toxic chemical which is widely used in various pharmaceutical, dye, and pigment industries. However, the excessive use of nitroaniline and its persistence in the environment poses a serious threat to the health and wellness of living organisms. Thus, due to its highly stable and toxic nature, it is essential to monitor the presence of nitroaniline in the environment. Among various methods used to monitor the toxic chemicals, electrochemical-based sensors devised from metal oxide are considered to be an important class of sensors which provide an effective, efficient, and selective response [33–36]. Herein, the fabrication and characterization of anatase-phase TiO_2 nanoflowers based on an efficient nitroaniline chemical sensor are reported.

2. Materials and Methods

2.1. TiO₂ Nanoflowers Synthesis

In a typical procedure, 0.04 M titanium chloride ($TiCl_4$, Samchun Chemicals, Daejeon, Korea) was slowly added to 50 mL of deionized (DI) water in an ice bath and stirred for 10 min. After complete mixing of $TiCl_4$, the reaction mixture was taken out of the ice bath and 50 mL DI water was added. A small amount (5 mL) of liquid ammonia (28% NH_3, Samchun Chemicals, Daejeon, Korea) was mixed in the reaction mixture under continuous stirring, and was placed in the laboratory oven at 70 °C for 6 h which resulted in white precipitate. Consequently, the obtained precipitate was washed properly by ethanol and DI water. Later, the washed precipitate was dried in the oven at 60 °C for

24 h and calcined at 450 °C for 2 h. The final product was then characterized by different techniques to investigate the morphological, structural, compositional, optical, photovoltaic, and sensing properties.

2.2. Characterizations of TiO$_2$ Nanoflowers

The morphologies of the synthesized TiO$_2$ nanoflowers were investigated using a field emission scanning electron microscope (FESEM, Hitachi S-4800, Tokyo, Japan), transmission electron microscope (TEM, JEM-ARM200F, JEOL, Peabody, MA, USA) and high-resolution (HR) TEM. The crystal and structural properties of the synthesized material were examined using X-ray diffraction (XRD, PANalyticalX'Pert PRO, Malvern Panalytical, Malvern, UK) and X-ray photoelectron spectroscopy (XPS, AXISNOVA CJ109, Kratos Inc., Manchester, UK). The XRD was measured in a range of 20–80° with Cu-Kα radiation (λ = 1.54178 Å). Energy-dispersive spectroscopy (EDS) connected with FESEM and Fourier transform infrared spectroscopy (FTIR, Nicolet, IR300, Thermo Fisher Scientific, Waltham, MA, USA) were used to observe the chemical and elemental compositions of the synthesized nanoflowers. The FTIR sample was prepared on KBr-based pellets and measured in the range 400–4000 cm^{-1}. Room-temperature Raman-scattering (Raman microscope, Renishaw, UK) and UV–Vis spectroscopic techniques (2550 Shimadzu, Kyoto, Japan) were used to examine scattering and optical properties, respectively.

2.3. Fabrication and Characterization of DSSC Based on TiO$_2$ Nanoflowers

The fabrication of a DSSC based on TiO$_2$ nanoflowers was done as reported elsewhere [22]. For the photoanode, a slurry of the synthesized TiO$_2$ nanoflower powder (0.2 g) was made by mixing it with aqueous polyethylene glycol (PEG, 4 wt.%) solution. An incremental addition of PEG solution was important to achieve a uniform TiO$_2$ slurry. The prepared TiO$_2$ slurry was spread by the doctor blade method over the framed fluorine-doped tin oxide (FTO) glass substrates and kept for 10 min to dry. Afterward, the TiO$_2$-coated FTO substrate was calcined at 450 °C for 30 min. Consequently, the TiO$_2$-coated FTO substrate was kept for dye absorption by immersing it into 0.3 mM ethanolic solution of N719 dye at room temperature for 16 h in the dark. After dye absorption of the required time, ethanol solvent was used to rinse the dye-absorbed TiO$_2$-coated FTO substrate and removed non-absorbed dye from the TiO$_2$ surface, and finally dried in an oven under nitrogen stream at 40 °C. To prepare the counter-electrode, a thin layer (~80 nm) of platinum (Pt) was coated with the ion sputtering technique on the cleaned FTO glass substrate. The DSSC assembly was made by combining the counter (Pt-coated FTO) and photoanode (dye-absorbed TiO$_2$-coated FTO) and sealed with a separating Surlyn sealing sheet (60 μm) using a hot plate. The redox electrolyte, made of 0.05 mM I$_2$, 0.2 M tert-butyl pyridine in acetonitrile, and 0.5 M LiI, was inserted through one of two small holes initially made on the counter electrode. The fabricated DSSC possessed an active area of 0.25 cm^2.

3. Results and Discussion

3.1. Crystalline and Structural Characterizations of TiO$_2$ Nanoflowers

The crystalline properties of the synthesized TiO$_2$ materials were examined by XRD analysis and the obtained diffraction peaks are demonstrated in Figure 1.
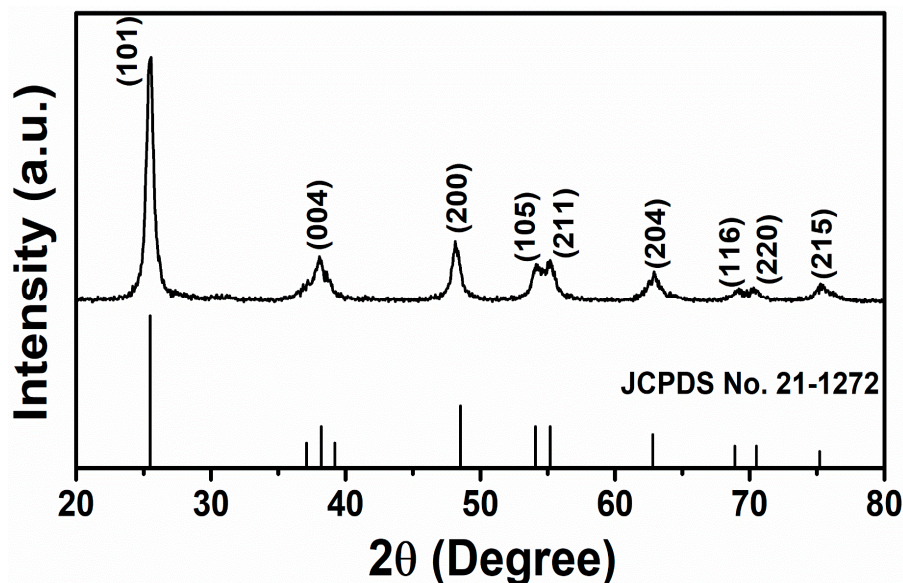
Figure 1. Typical XRD patterns of TiO$_2$ nanoflowers synthesized by facile low-temperature solution process.

The diffraction pattern of synthesized TiO$_2$ constituted several well-defined peaks which were located at 2θ = 25.4°, 38.1°, 48°, 54.1°, 55.2°, 62.7°, 68.9°, 70.5°, and 75.2° and assigned as the lattice places of TiO$_2$ (101), (004), (200), (105), (211), (204), (116), (220), and (215), respectively. The observed diffraction peaks were assigned to the typical TiO$_2$ tetragonal crystal phase corresponding to anatase (JCPDS 21-1272) [37,38]. The crystallite size and full width half maxima (FWHMs) of synthesized TiO$_2$ powders were accounted by Scherrer's equation [39]. Using the diffraction peak at 25.4°, the synthesized TiO$_2$ powders showed a small crystallite size of 12.23 nm and FWHM value of 0.7°. Other peaks corresponding to other crystalline forms or any other material were not observed, suggesting that the synthesized TiO$_2$ was composed of pure anatase phase.

The morphology of synthesized TiO$_2$ powders was investigated by performing the FESEM and TEM analysis. Figure 2a–c shows the FESEM images of the synthesized TiO$_2$. At low magnification (Figure 2a,b), it could be well-observed that the synthesized TiO$_2$ materials possessed a flower-like morphology and had grown in high density. The magnified FESEM image (Figure 2c) revealed that several rod-like structures with an average length of ~100 nm aggregated in three dimensions to form a flower-like morphology. The elemental composition of the synthesized TiO$_2$ nanoflowers were observed from the EDS spectrum, as shown in Figure 2d. The prominent element peaks of Ti and O are seen in Figure 2d, which suggests that the synthesized materials were composed of only Ti and O. From quantitative analysis, the stoichiometric atomic weight % ratio of each element (83.69% for O and 16.31% for Ti) clearly confirms the formation of TiO$_2$. No other peaks were seen for other any other element, suggesting the high purity of the TiO$_2$ nanoflowers.

Synthesized TiO$_2$ morphology was analyzed again by TEM and HRTEM analysis, as indicated in Figure 3. The low-resolution TEM image (Figure 3a) of the synthesized TiO$_2$ clearly shows rods like petals which are aggregated to form a three-dimensional flower-like morphology. Flower-like TiO$_2$ is in the nano-dimension, and it was estimated that each petal (rod) had an average size of ≤100 nm. Hence, the results of TEM were in accordance with the FESEM images. The HRTEM image (Figure 3b) presented well-defined lattice fringes with a difference in lattice spacing of 0.35 nm, that is promptly evidenced the typical lattice spacing of the (110) plane of anatase TiO$_2$ [40,41]. Figure 3c depicts the selected area electron diffraction (SAED) patterns of as-synthesized TiO$_2$ nanoflowers. SEAD patterns are the ring-like patterns which indicate the polycrystalline nature of TiO$_2$.
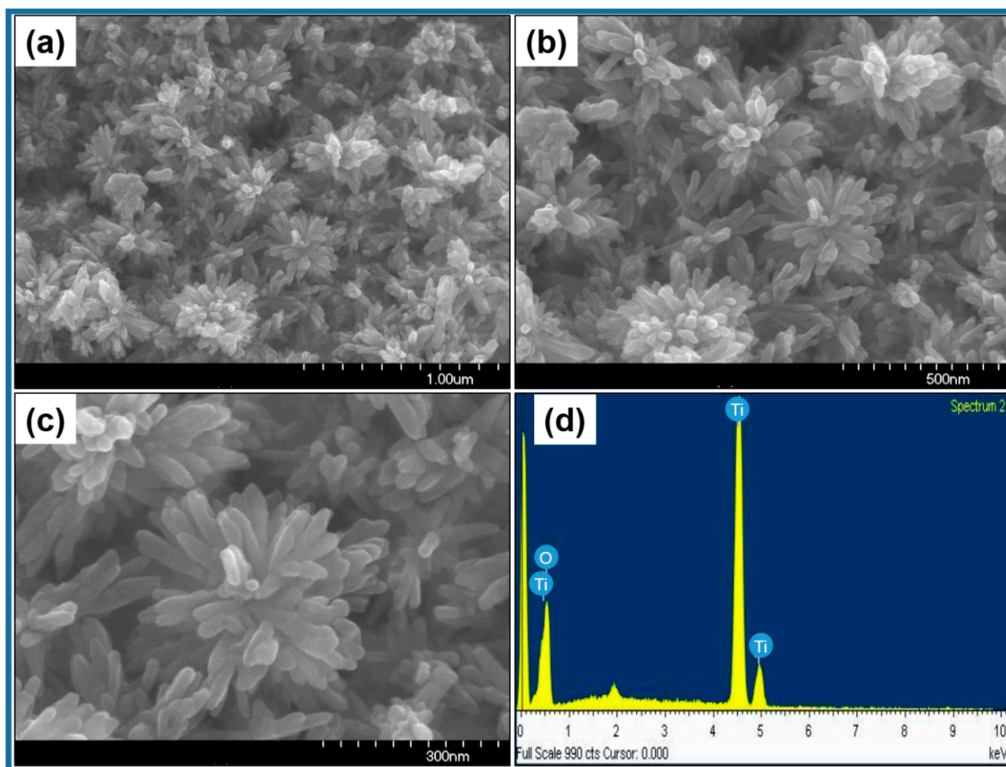
Figure 2. (**a**–**c**) FESEM images and (**d**) EDS spectrum of TiO$_2$ nanoflowers synthesized by facile low-temperature solution process.
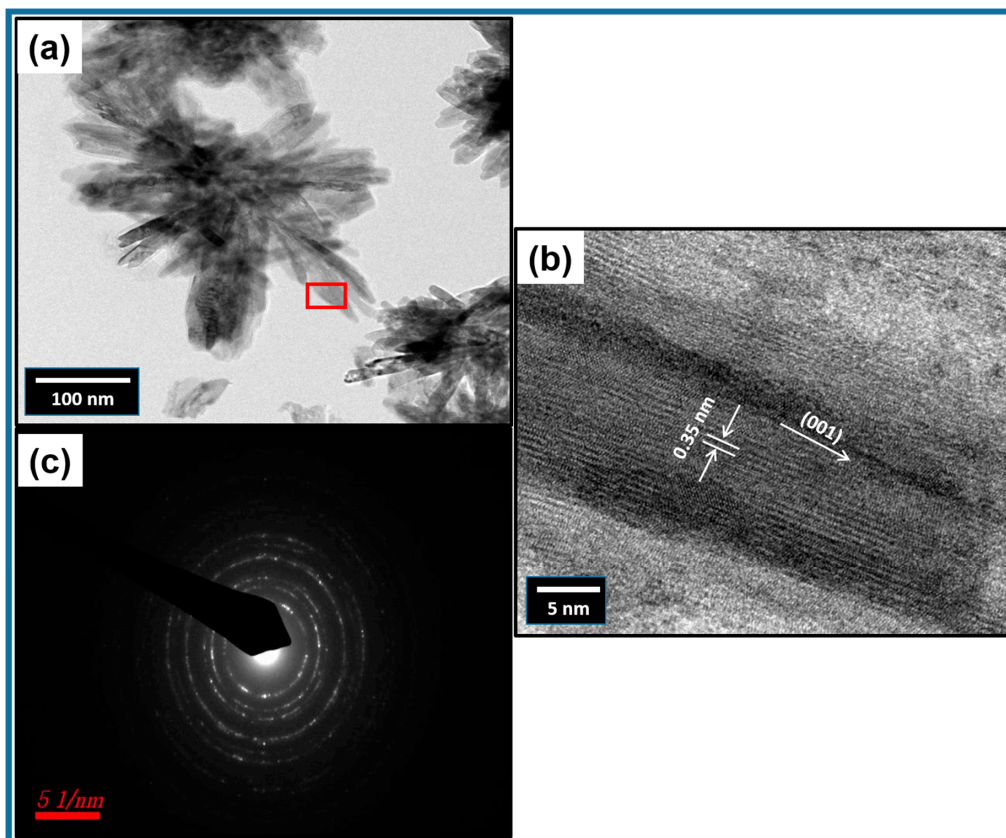

Figure 3. Typical (**a**) TEM, (**b**) HRTEM, and (**c**) SAED pattern of TiO$_2$ nanoflowers synthesized by facile low-temperature solution process.

The optical properties of the synthesized TiO_2 nanoflowers were investigated using UV–Vis spectroscopy, as indicated in Figure 4a. The synthesized TiO_2 nanoflowers exhibited an absorption edge at 398 nm, which corresponded to an energy band gap of 3.2 eV. The obtained band gap value was well matched with the value of typical anatase TiO_2 (i.e., E_g = 3.21 eV). Hence, from UV–Vis spectroscopic studies, it was again confirmed that the synthesized material was pure anatase TiO_2. Moreover, the typical FTIR spectrum was also recorded in the range from 4000–400 cm^{-1} for the synthesized TiO_2 nanoflowers to explain their structural properties. Figure 4b shows the synthesized TiO_2 nanoflower FTIR spectrum. The peaks located at 3430 and 1634 cm^{-1} originated from the surface OH groups and H–O–H bending vibration of adsorbed water, respectively [42]. A very intense IR band located at 547 cm^{-1} was assigned to the Ti–O stretching in TiO_2 lattice [42,43], which suggested the structure of TiO_2. Raman scattering spectroscopy was used to further investigate the structural and scattering properties of the synthesized TiO_2 nanoflowers in the range 100–800 cm^{-1} (Figure 4c). All the observed Raman bands in the range of 100–800 cm^{-1} corresponded to the representative peaks of O–Ti–O in TiO_2 nano-materials [44]. The appearance of the Raman band at 148 cm^{-1} was indicative of anatase TiO_2 [45]. Moreover, Raman bands at 634 cm^{-1} (E_g mode), 401 cm^{-1} (B_{1g}), and 516 cm^{-1} (doublet of A_{1g} and B_{1g} modes) were associated to symmetric Ti–O vibration from the A_g symmetric modes of the TiO_6 octahedra and the splitting of the degenerate mode of TiO_6 octahedra [45]. The obtained results were typical for the anatase phase of TiO_2 [44,45].
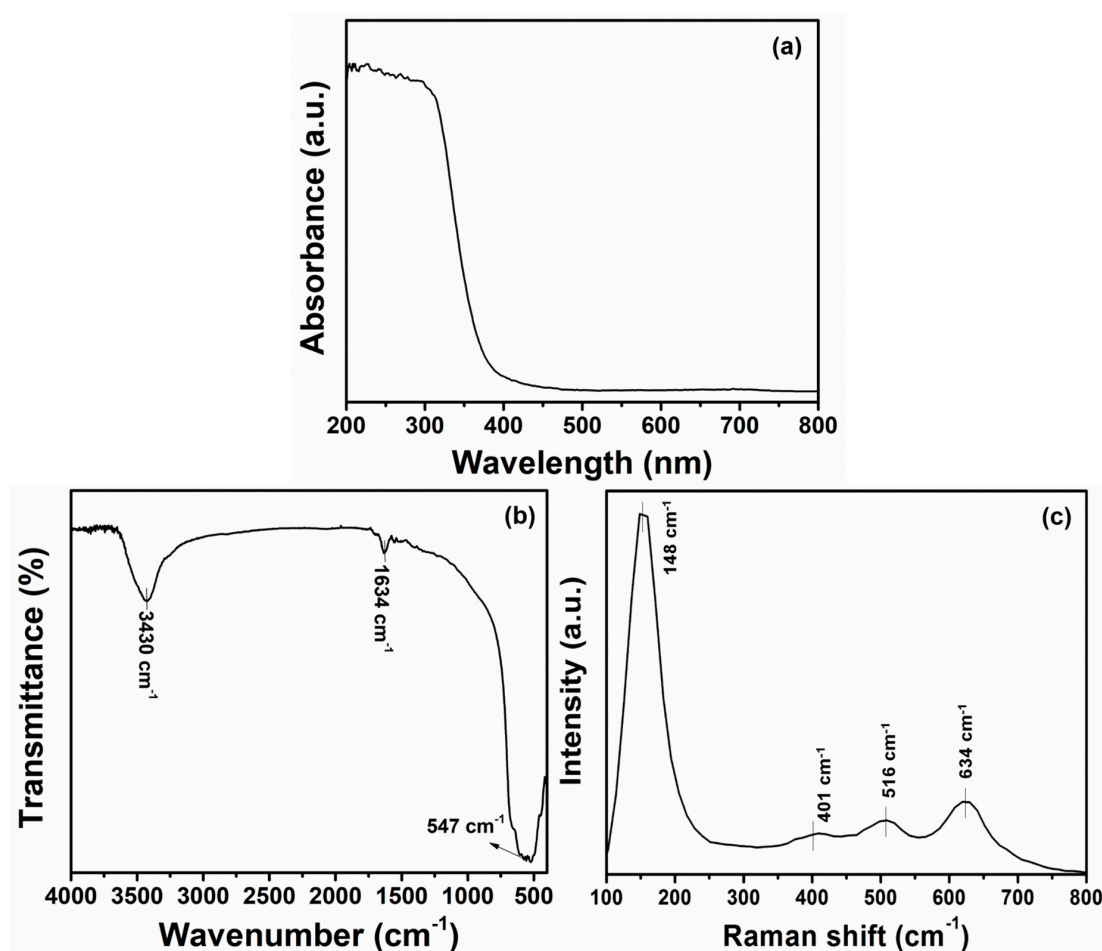
Figure 4. Typical (**a**) UV–Visible, (**b**) FTIR, and (**c**) Raman-scattering spectroscopy of synthesized TiO_2 nanoflowers.

Further, to examine the surface composition, electronic environment, and oxidation states, XPS analysis was performed for the synthesized nanoflowers. As is known in the spectrum of the

synthesized TiO$_2$ nanoflowers, well-defined corresponding peaks of Ti, O, and C were obtained. A peak for C 1s at a binding energy of 284 eV was seen, attributable to the adventitious hydrocarbon from the XPS instrument. Figure 5b shows the core element XPS spectra for the Ti 2p binding energy region. The Ti 2p$^{3/2}$ and Ti 2p$^{1/2}$ spin-orbital splitting photoelectrons for the synthesized TiO$_2$ nanoflowers specimen were seen at the binding energies of 456.8 and 462.3 eV, respectively. From the core element XPS spectrum for the O (1s) binding energy region (Figure 5c), it was observed that the peak corresponding to 529 eV corresponded to the lattice O of the TiO$_2$ lattice. Two binding energies located at 530.3 and 531.5 eV originated from the adsorbed moisture (expressed by TiOH) and oxygen deficiencies or oxygen vacancies (expressed by TiOH) over the TiO$_2$ surfaces. The existence of these defects (e.g., TiOH groups might helpful for the generation of oxygenated species such as hydroxyl ions, etc.) might take part in defining the sensing performance. With these observations, it is clear that the synthesized materials were again deduced to be anatase TiO$_2$ nanoflowers.
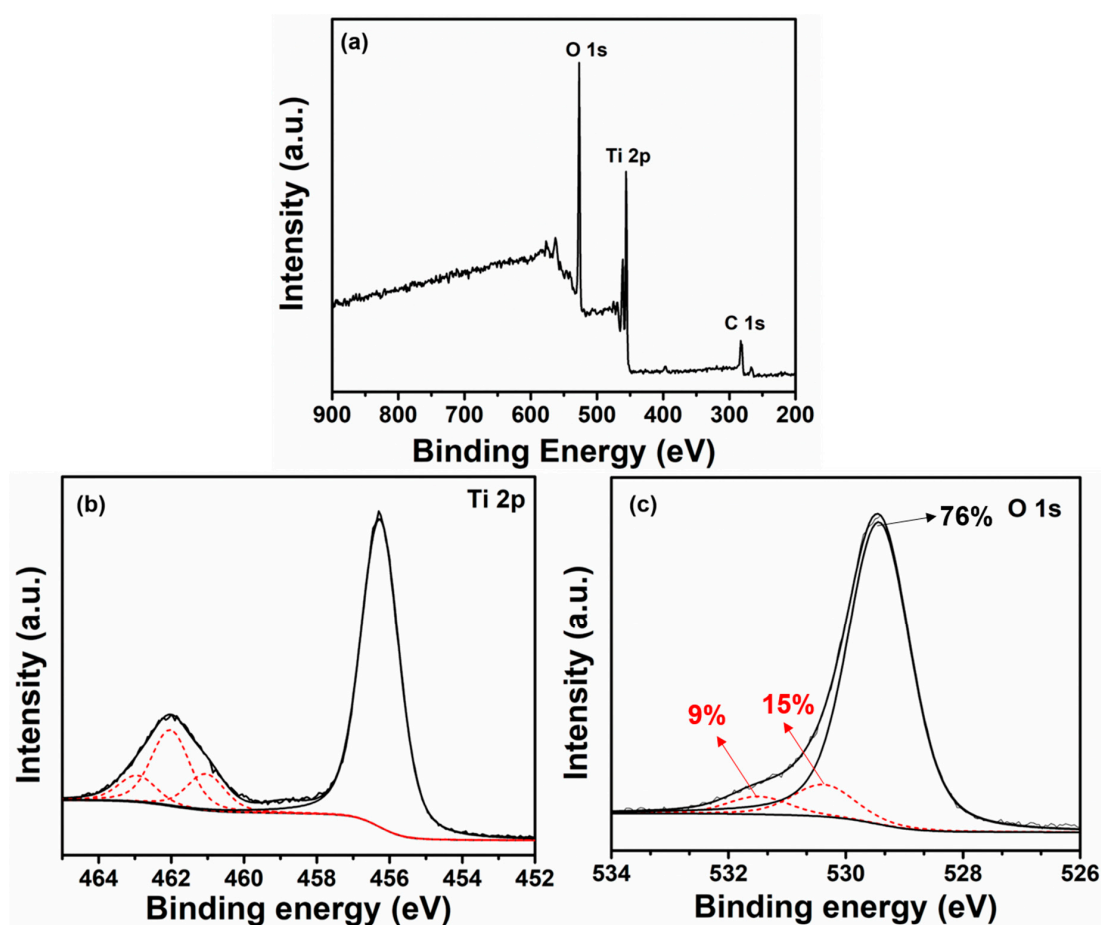

Figure 5. Typical XPS spectra of (**a**) survey, (**b**) deconvoluted high-resolution Ti 2p, and (**c**) deconvoluted high-resolution O 1s plots of as-synthesized TiO$_2$ nanoflowers.

The as-synthesized TiO$_2$ nanoflowers were further analyzed by measuring the N$_2$ adsorption–desorption isotherms to elucidate the specific surface area and pore size distribution. As shown in Figure 6, the obtained isotherm displayed a hysteresis loop in the relative pressure ranging from 0.4–0.9. Isotherms were analyzed using Brunauer-Emmett-Teller (BET, Micromeritics Tristar 3000, Norcross, GA, USA) analysis, and as-synthesized TiO$_2$ nanoflowers showed a specific surface area of ~63.34 m^2/g. A pore size distribution plot is presented in the inset of Figure 6. It indicates that as-synthesized TiO$_2$ nanoflowers developed mesopores, as observed by the distribution in the range of 5–20 nm. This result clearly displays the porous nature of as-synthesized TiO$_2$ nanoflowers, which could be helpful for high dye absorption and the generation of large oxygenated species.
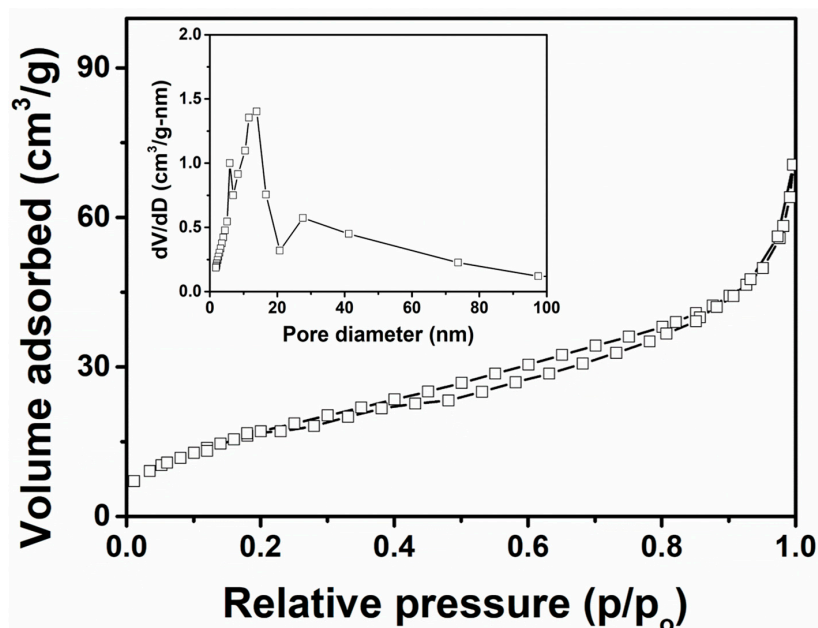
Figure 6. Nitrogen adsorption–desorption isotherms and pore-size distributions (inset) of as-synthesized TiO_2 nanoflowers.

3.2. Characterizations of TiO_2 Nanoflowers-Based DSSC

In order to evaluate the photovoltaic properties of the synthesized TiO_2 nanoflower-based photoanode, the photocurrent density (J)–voltage (V) of the fabricated DSSC was tested under 100 mW/cm^2 light illumination (1 sun). Figure 7a shows the J–V curve of the fabricated DSSC with the synthesized TiO_2 nanoflower-based photoanode. The fabricated DSSC yielded an overall conversion efficiency of ~3.64% along with a fill factor (FF) of ~0.67, open circuit voltage (V_{OC}) of 0.693 V, and short circuit current density J_{SC} of ~7.80 mA cm^{-2}. The high V_{OC} and FF of the device might be related to the generation of large grain sizes in the TiO_2 nanoflower thin film, which resulted in the slightly high recombination rate at the interface of the TiO_2 nanoflower/electrolyte. The low J_{SC} obtained by fabricated DSSC was associated with the low surface area of TiO_2 nanoflowers (BET surface area = 63.34 m^2/g), which might induce the light harvesting efficiency. To support low light harvesting efficiency and low J_{SC}, an incident photon to current efficiency (IPCE) curve of the fabricated DSSC with synthesized TiO_2 nanoflower based photoanode was investigated as a function of wavelength. Figure 7b depicts the IPCE curve of the fabricated DSSC with the synthesized TiO_2 nanoflower-based photoanode in a wavelength range of 300–800 nm. The maximum IPCE was observed to be ~41% at 540 nm wavelength for the fabricated DSSC. From the IPCE curve, the estimated integrated J_{SC} value was 8.12 mA/cm^2, which is in excellent agreement with the J_{SC} value obtained from the J–V curve. It was assumed that the TiO_2 nanoflowers thin film poses a less-porous surface for dye loading, resulting in a low injection rate and high electron recombination. These factors might have retarded the photovoltaic performance and photocurrent density of the fabricated DSSC, and resulted in the low IPCE and low light harvesting efficiency. Zalas, M. et al. reported the fabrication of a DSSC based on TiO_2 material which exhibited a photon-to-current efficiency of ~0.47% [46]. Similarly, Jang et al. demonstrated the use of an Al-incorporated TiO_2 layer for a dye-sensitized solar cell application which exhibited an overall power conversion efficiency of ~2.81% [47]. Hu et al. presented the photo deposition of Ag nanoparticles on branched TiO_2 nanorod arrays for dye-sensitized solar cells which presented light-to-electricity conversion efficiencies in the range of 1.87–2.83% [48]. Even though the performance was reasonable, the TiO_2 nanoflower-based photoanode (in our case) showed higher photovoltaic performance when compared to similar photoanode based DSSCs in other scientific literature [44,46–48].
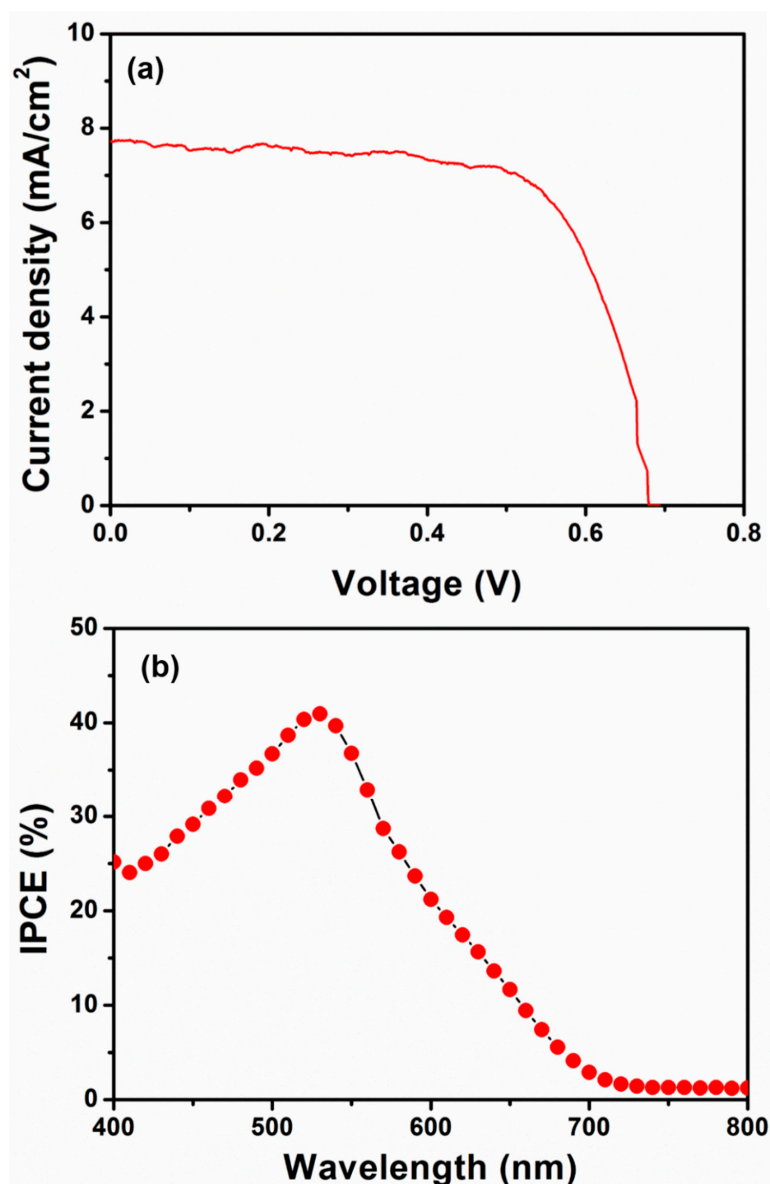
Figure 7. Typical (**a**) current–voltage (J–V) and (**b**) incident photon to current efficiency (IPCE) characteristics of TiO$_2$ nanoflowers-based dye-sensitized solar cells.

3.3. Properties of Nitroaniline Chemical Sensor Based on TiO$_2$ Nanoflowers

To fabricate the nitroaniline chemical sensor, a glassy carbon electrode (GCE) was modified with TiO$_2$ nanoflowers which acted as an electron mediator material. The nitroaniline chemical sensor was designed in such a way that the TiO$_2$ nanoflowers-modified GCE was used as a working electrode, while Pt wire acted as a counter-electrode in the phosphate buffer solution (PBS, 0.1 M). The effect of nitroaniline concentrations (0.5–60 mM) was studied by examining the I–V characteristics of several nitroaniline concentrations in PBS solution (pH = 7) at room temperature (298 K) with a relative humidity of 28%. From Figure 8a, the TiO$_2$-nanoflower modified GCE exhibited a quick current response after the addition of a very low nitroaniline concentration in 1 M PBS, which clearly suggested a good electrochemical response towards nitroaniline. A series of I–V curves were performed with the TiO$_2$ nanoflower-modified GCE with the different nitroaniline concentrations in 1 M PBS using the applied potential range from 0–1.5 V. As indicated in Figure 8a, with the increase in nitroaniline concentration, there was an increase in current response that could be attributed to the solution ionic strength improvement. This phenomenon proves very promising to increase the

conductivity of chemo-sensors based on TiO_2 nanoflowers. For detailed sensing parameters, the calibration plot for current vs. nitroaniline concentration was drawn from Figure 8a, as shown in Figure 8b. The current was linearly increased up to 6 mM afterward, and had a saturation level, which indicated the non-availability of ions at a higher nitroaniline concentration. Importantly, the chemo-sensor based on TiO_2 nanoflowers expressed good linearity from 0.5–6 mM. A relatively high sensitivity of 268.9 µA mM^{-1} cm^{-2} along with a detection limit as low as 1.05 mM and response time (10 s) were attained by the fabricated nitroaniline sensor with a TiO_2 nanoflowers-modified GCE. The good sensitivity and linearity over the TiO_2 nanoflowers-modified GCE for nitroaniline sensing may be correlated with the specific flower morphology, which possessed superior surface-to-volume ratio, and thus exhibited very good adsorption and better electro-catalytic activities. The good sensing behavior of TiO_2 nanoflowers-modified GCE can further be explained by understanding the sensing mechanism over the electrode surface.
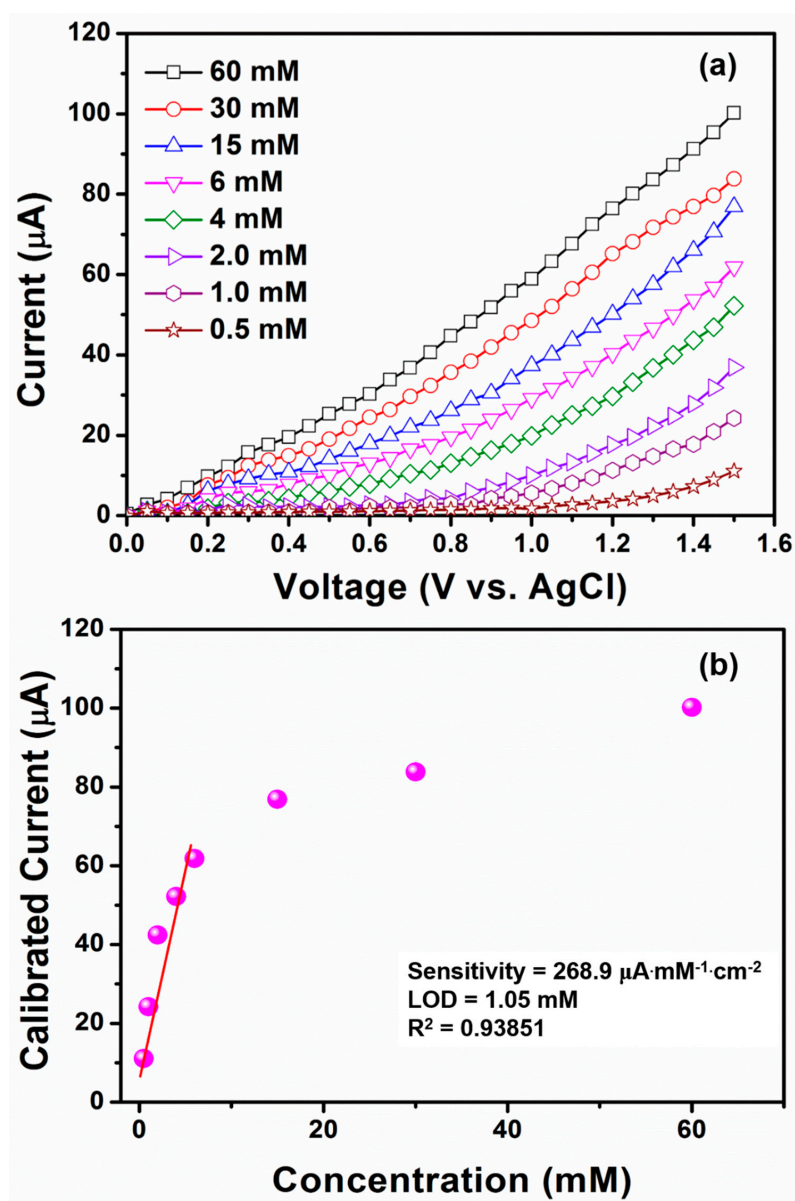

Figure 8. Typical (**a**) concentration-dependent (concentrations of 60–0.5 mM in 0.1 M PBS) I–V response of the fabricated TiO_2 nanoflowers-based nitroaniline chemical sensor; (**b**) corresponding graph for calibration current vs. concentration of nitroaniline.

Figure 9 shows the illustration of a possible mechanism for sensing response toward nitroaniline over the TiO_2 nanoflowers-modified GCE. In the beginning of the sensing process, the TiO_2 nanoflowers-modified GCE was primarily socialized with atmospheric oxygen molecules by taking an electron from the conduction band of TiO_2. This process produced numerous active oxygen species, such as HO^-, O^-, O_2^-, etc. [49], as presented in Figure 9. These generated oxygen species were responsible for the chemisorption of nitroaniline chemical over the surface of the TiO_2 nanoflowers-modified GCE. After interaction with the electrode surface, the nitroaniline chemical immediately oxidized into nitrosoaniline by leaving the electron on the surface of the TiO_2 nanoflowers-modified GCE. Thus, the sensing properties of the TiO_2 nanoflowers-modified GCE-based sensor was basically based on the good surface and electronic properties of TiO_2 and the redox reactions that took place during the electrochemical measurement.
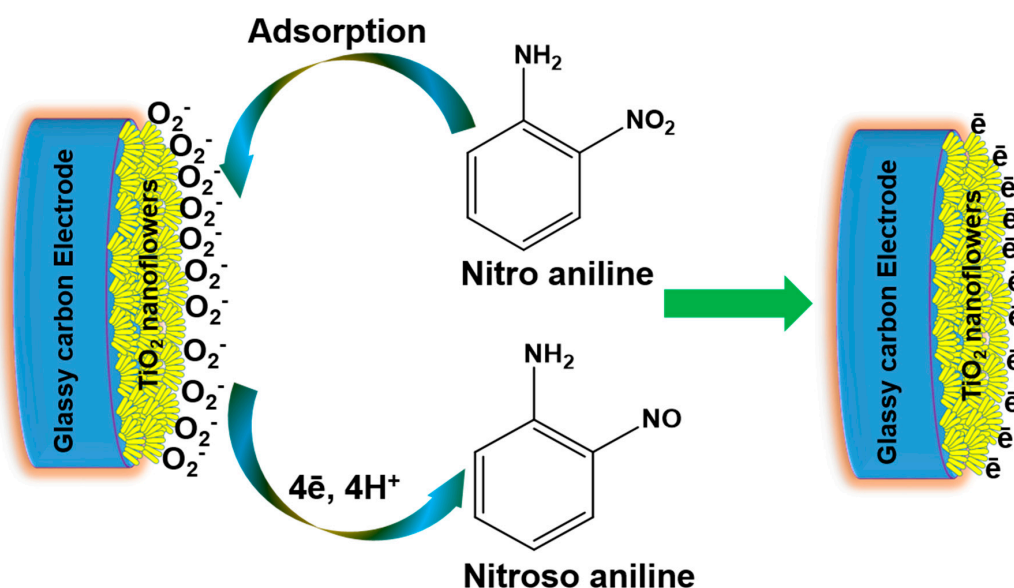

Figure 9. Illustration of possible nitroaniline chemical sensing over TiO_2 nanoflowers-modified glassy carbon electrode (GCE).

4. Conclusions

In summary, TiO_2 nanostructures with flowerlike morphology and high crystallinity were synthesized using a facile chemical precipitation method. It was found that petal-like rods aggregated to form three-dimensional flower-like structures, grown in high density. In order to study the synthesized material surface composition, XPS studies were conducted and it was confirmed that highly pure TiO_2 composed of Ti and O was prepared. The UV–Vis spectroscopic studies confirmed the preparation of anatase TiO_2 with λ_{max} 398 nm, corresponding to an energy band gap of 3.2 eV. The synthesized TiO_2 nanoflowers were used in the fabrication of a DSSC as photoanode materials, and achieved an overall efficiency of 3.64% with a maximum IPCE of ~41% at 540 nm wavelength. The synthesized TiO_2 nanoflowers were also used for the electrochemical sensing of nitroaniline. The fabricated nitroaniline sensor with a TiO_2 nanoflowers-modified GCE exhibited a sensitivity of 268.9 $\mu A\ mM^{-1}\ cm^{-2}$ and a detection limit as low as 1.05 mM with a short response time. From this study, it is confirmed that the reported synthesis route is a facile method for the preparation of TiO_2 with flower-like morphology and high crystallinity, which has great prospects in DSSCs and electro-chemical sensors.

Author Contributions: A.U., M.S.A. and I.J., conceived and designed the experiments; A.U., M.S.A., and I.J. performed the experiments, A.U., M.S.A., S.S., and I.J. analyzed the data contributed reagents/materials/analysis tools and wrote the paper. A.U., M.S.A., S.S., I.J., H.H.H., and H.A. read and revised the paper.

Conflicts of Interest: The authors declare no conflict of interest.

References

1.   Tian, C.; Zhang, Q.; Wu, A.; Jiang, M.; Liang, Z.; Jiang, B.; Fu, H. Cost-effective large-scale synthesis of ZnO photocatalyst with excellent performance for dye photodegradation. *Chem. Commun.* **2012**, *48*, 2858–2860. [CrossRef]

2.   Ansari, S.A.; Khatoon, Z.; Parveen, N.; Fouad, H.; Kulkarni, A.; Umar, A.; Ansari, Z.A.; Ansari, S.G. Polyaniline-Functionalized TiO_2 Nanoparticles as a Suitable Matrix for Hydroquinone Sensor. *Sci. Adv. Mater.* **2017**, *9*, 2032–2038. [CrossRef]

3.   Kulal, P.M.; Dubal, D.P.; Lokhande, C.D.; Fulari, V.J. Chemical synthesis of Fe_2O_3 thin films for supercapacitor application. *J. Alloys Compd.* **2011**, *509*, 2567–2571. [CrossRef]

4.   Chen, W.; Peng, S.; Tang, S.; Jin, L.; Zhou, Q. Palladium Doped SnO_2 Nanocrystals for Enhanced Methane Gas Sensing Application. *Sci. Adv. Mater.* **2017**, *9*, 1735–1741. [CrossRef]

5.   Sood, S.; Kumar, S.; Umar, A.; Kaur, A.; Mehta, S.K.; Kansal, S.K. TiO_2 quantum dots for the photocatalytic degradation of indigo carmine dye. *J. Alloys Compd.* **2015**, *650*, 193–198. [CrossRef]

6.   Wang, Y.Q.; Gu, L.; Guo, Y.G.; Li, H.; He, X.Q.; Tsukimoto, S.; Ikuhara, Y.; Wan, L.J. Rutile-TiO_2 nanocoating for a high-rate $Li_4Ti_5O_{12}$ anode of a lithium-ion battery. *J. Am. Chem. Soc.* **2012**, *134*, 7874–7879. [CrossRef]

7.   O'regan, B.; Grätzel, M. A low-cost, high-efficiency solar cell based on dye-sensitized colloidal TiO_2 films. *Nature* **1991**, *353*, 737. [CrossRef]

8.   Hara, K.; Sayama, K.; Ohga, Y.; Shinpo, A.; Suga, S.; Arakawa, H. A coumarin-derivative dye sensitized nanocrystalline TiO_2 solar cell having a high solar-energy conversion efficiency up to 5.6%. *Chem. Commun.* **2001**, *6*, 569–570. [CrossRef]

9.   Shin, S.G.; Bark, C.W.; Kim, S.M.; Choi, H.W. Properties of Perovskite Solar Cells by the Sputtered Compact TiO_2 Layer. *Sci. Adv. Mater.* **2017**, *9*, 1517–1521. [CrossRef]

10. Zhuge, F.; Qiu, J.; Li, X.; Gao, X.; Gan, X.; Yu, W. Toward Hierarchical TiO_2 Nanotube Arrays for Efficient Dye-Sensitized Solar Cells. *Adv. Mater.* **2011**, *23*, 1330–1334. [CrossRef]

11. Tang, Y.; Wee, P.; Lai, Y.; Wang, X.; Gong, D.; Kanhere, P.; Lim, T.; Dong, Z.; Chen, Z. Hierarchical TiO_2 Nanoflakes and Nanoparticles Hybrid Structure for Improved Photocatalytic Activity. *J. Phys. Chem. C* **2012**, *116*, 2772–2780. [CrossRef]

12. Bai, H.; Liu, Z.; Liu, L.; Sun, D. Large-Scale Production of Hierarchical TiO_2 Nanorod Spheres for Photocatalytic Elimination of Contaminants and Killing Bacteria. *Chem. Eur. J.* **2013**, *19*, 3061–3070. [CrossRef]

13. Lü, X.; Ding, S.; Xie, Y.; Huang, F. Non-Aqueous Preparation of High-Crystallinity Hierarchical TiO_2 Hollow Spheres with Excellent Photocatalytic Efficiency. *Eur. J. Inorg. Chem.* **2011**, *18*, 2879–2883. [CrossRef]

14. Xiang, L.; Zhao, X.; Yin, J.; Fan, B. Well-organized 3D urchin-like hierarchical TiO_2 microspheres with high photocatalytic activity. *J. Mater. Sci.* **2012**, *47*, 1436–1445. [CrossRef]

15. Chen, Y.; Li, A.; Li, Q.; Hou, X.; Wang, L.; Huang, Z. Facile fabrication of three-dimensional interconnected nanoporous N-TiO_2 for efficient photoelectrochemical water splitting. *J. Mater. Sci. Technol.* **2018**, *34*, 955–960. [CrossRef]

16. Li, Z.; Mo, L.; Chen, W.; Shi, X.; Wang, N.; Hu, L.; Hayat, T.; Alsaedi, A.; Dai, S. Solvothermal Synthesis of Hierarchical TiO2 Microstructures with High Crystallinity and Superior Light Scattering for High-Performance Dye-Sensitized Solar Cells. *ACS Appl. Mater. Int.* **2017**, *9*, 32026–32033. [CrossRef]

17. Ghosh, M.; Liu, J.; Chuang, S.S.C.; Jana, S.C. Fabrication of Hierarchical V_2O_5 Nanorods on TiO_2 Nanofibers and Their Enhanced Photocatalytic Activity under Visible Light. *ChemCatChem* **2018**, *10*, 3305. [CrossRef]

18. Liu, H.; Zhang, L.; Li, T. A Study of Controllable Synthesis and Formation Mechanism on Flower-Like TiO_2 with Spherical Structure. *Crystals* **2018**, *8*, 466. [CrossRef]

19. Hu, J.; Zhao, L.; Yang, Y.; Wang, S.; Liao, H.; Sun, X.; Tong, S.Q.; Dong, B. Influence of Anodization Voltage on Photovoltaic Performance of Dye-Sensitized Solar Cells Based on TiO$_2$ Nanotube Array. *Sci. Adv. Mater.* **2017**, *9*, 641–648. [CrossRef]

20. Ko, K.H.; Lee, Y.C.; Jung, Y.J. Enhanced efficiency of dye-sensitized TiO$_2$ solar cells (DSSC) by doping of metal ions. *J. Colloid Interface Sci.* **2005**, *283*, 482–487. [CrossRef]

21. Peng, L.; Tang, A.W.; Jia, X.; Pan, L.; Zou, J.J. Surfactant-Assisted Synthesis and Photocatalytic Activity of Anatase TiO$_2$ Nanocrystals. *Sci. Adv. Mater.* **2017**, *9*, 782–789. [CrossRef]

22. Umar, A.; Akhtar, M.S.; Al-Assiri, M.S.; Al-Salami, A.E.; Kim, S.H. Composite CdO-ZnO hexagonal nanocones: Efficient materials for photovoltaic and sensing applications. *Ceram. Int.* **2018**, *44*, 5017–5024. [CrossRef]

23. Kontos, A.I.; Kontos, A.G.; Tsoukleris, D.S.; Bernard, M.C.; Spyrellis, N.; Falaras, P. Nanostructured TiO$_2$ films for DSSCS prepared by combining doctor-blade and sol–gel techniques. *J. Mater. Process. Technol.* **2008**, *196*, 243–248. [CrossRef]

24. Zhang, H.; Han, Y.; Liu, X.; Liu, P.; Yu, H.; Zhang, S.; Yao, X.; Zhao, H. Anatase TiO$_2$ microspheres with exposed mirror-like plane {001} facets for high performance dye-sensitized solar cells (DSSCs). *Chem. Commun.* **2010**, *46*, 8395–8397. [CrossRef]

25. Yang, R.; Cai, J.; Lv, K.; Wu, X.; Wang, W.; Xu, Z.; Li, M.; Li, Q.; Xu, W. Fabrication of TiO$_2$ hollow microspheres assembly from nanosheets (TiO$_2$-HMSs-NSs) with enhanced photoelectric conversion efficiency in DSSCs and photocatalytic activity. *Appl. Catal. B* **2017**, *210*, 184–193. [CrossRef]

26. Skubal, L.R.; Meshkov, N.K.; Vogt, M.C. Detection and identification of gaseous organics using a TiO$_2$ sensor. *J. Photochem. Photobiol. A* **2002**, *148*, 103–108. [CrossRef]

27. Mabrook, M.; Hawkins, P. A rapidly-responding sensor for benzene, methanol and ethanol vapours based on films of titanium dioxide dispersed in a polymer operating at room temperature. *Sens. Actuators B* **2001**, *75*, 197–202. [CrossRef]

28. Zhu, B.L.; Xie, C.S.; Wang, W.Y.; Huang, K.J.; Hu, J.H. Improvement in gas sensitivity of ZnO thick film to volatile organic compounds (VOCs) by adding TiO$_2$. *Mater. Lett.* **2004**, *58*, 624–629. [CrossRef]

29. Wen, Z.; Tian-Mo, L. Gas-sensing properties of SnO$_2$–TiO$_2$-based sensor for volatile organic compound gas and its sensing mechanism. *Physica B* **2010**, *405*, 1345–1348. [CrossRef]

30. Zhang, Y.; Li, D.; Qin, L.; Liu, D.; Liu, Y.; Liu, F.; Song, H.; Wang, Y.; Lu, G. Preparation of Au-loaded TiO$_2$ pecan-kernel-like and its enhanced toluene sensing performance. *Sens. Actuators B* **2018**, *255*, 2240–2247. [CrossRef]

31. Malik, R.; Tomer, V.K.; Chaudhary, V.; Dahiya, M.S.; Nehra, S.P.; Rana, P.S.; Duhan, S. Ordered mesoporous In-(TiO$_2$/WO$_3$) nanohybrid: An ultrasensitive n-butanol sensor. *Sens. Actuators B* **2017**, *239*, 364–373. [CrossRef]

32. Ghosh, M.; Lohrasbi, M.; Chuang, S.S.C.; Jana, S.C. Mesoporous Titanium Dioxide Nanofibers with a Significantly Enhanced Photocatalytic Activity. *ChemCatChem* **2016**, *8*, 2525. [CrossRef]

33. Ahmad, R.; Tripathy, N.; Ahn, M.S.; Hahn, Y.B. Development of highly-stable binder-free chemical sensor electrodes for p-nitroaniline detection. *J. Colloid Interface Sci.* **2017**, *494*, 300–306. [CrossRef]

34. Ibrahim, A.A.; Umar, A.; Baskoutas, S. Ytterbium Doped Zinc Oxide Nanopencils for Chemical Sensor Application. *J. Nanosci. Nanotechnol.* **2017**, *17*, 9157–9162. [CrossRef]

35. Ahmad, N.; Umar, A.; Kumar, R.; Alam, M. Microwave-assisted synthesis of ZnO doped CeO$_2$ nanoparticles as potential scaffold for highly sensitive nitroaniline chemical sensor. *Ceram. Int.* **2016**, *42*, 11562–11567. [CrossRef]

36. Yu, Z.; Wang, F.; Lin, X.; Wang, C.; Fu, Y.; Wang, X.; Zhao, Y.; Li, G. Selective fluorescence sensors for detection of nitroaniline and metal Ions based on ligand-based luminescent metal-organic frameworks. *J. Solid State Chem.* **2015**, *232*, 96–101. [CrossRef]

37. Sood, S.; Mehta, S.K.; Umar, A.; Kansal, S.K. The visible light-driven photocatalytic degradation of Alizarin red S using Bi-doped TiO$_2$ nanoparticles. *New J. Chem.* **2014**, *38*, 3127–3136. [CrossRef]

38. Yadav, H.M.; Kim, J.S. Sol-Gel Synthesis of Co^{2+}-Doped TiO$_2$ Nanoparticles and Their Photocatalytic Activity Study. *Sci. Adv. Mater.* **2017**, *9*, 1114–1119. [CrossRef]

39. Zhou, Y.C.; Rahaman, M.N. Hydrothermal synthesis and sintering of ultrafine CeO$_2$ powders. *J. Mater. Res.* **1993**, *8*, 1680. [CrossRef]

40. Kusior, A.; Banas, J.; Trenczek-Zajac, A.; Zubrzycka, P.; Micek-Ilnicka, A.; Radecka, M. Structural properties of TiO_2 nanomaterials. *J. Mol. Struct.* **2018**, *1157*, 327–336. [CrossRef]

41. Rajender, G.; Kumar, J.; Giri, P.K. Interfacial charge transfer in oxygen deficient TiO_2-graphene quantum dot hybrid and its influence on the enhanced visible light photocatalysis. *Appl. Catal. B* **2018**, *224*, 960–972. [CrossRef]

42. Razali, M.H.; Noor, A.F.M.; Yusoff, M. Hydrothermal Synthesis and Characterization of Cu^{2+}/F^- Co-Doped Titanium Dioxide (TiO_2) Nanotubes as Photocatalyst for Methyl Orange Degradation. *Sci. Adv. Mater.* **2017**, *9*, 1032–1041. [CrossRef]

43. Kim, T.H.; Jeong, H.G.; Park, D.W. Crystal Phase Control Process of Anatase and Rutile TiO_2 Nanopowder by Thermal Plasma. *Sci. Adv. Mater.* **2017**, *9*, 1637–1643. [CrossRef]

44. Shalini, S.; Balasundaraprabhu, R.; Kumar, T.S.; Muthukumarasamy, N.; Prasanna, S.; Sivakumaran, K.; Kannan, M.D. Enhanced performance of sodium doped TiO_2 nanorods based dye sensitized solar cells sensitized with extract from petals of Hibiscus sabdariffa (Roselle). *Mater. Lett.* **2018**, *221*, 192–195. [CrossRef]

45. Ameen, S.; Akhtar, M.S.; Seo, H.K.; Shin, H.S. TiO_2 nanotube arrays via electrochemical anodic oxidation: Prospective electrode for sensing phenyl hydrazine. *Appl. Phys. Lett.* **2013**, *103*, 061602. [CrossRef]

46. Zalas, M.; Cynarzewska, A. Application of paper industry waste materials containing TiO_2 for dye-sensitized solar cells fabrication. *Optik* **2018**, *158*, 469–476. [CrossRef]

47. Jang, B.Y.; Lee, M.; Kim, J.H.; Ahn, K.S.; Han, Y.S. Effects of an Al-Incorporated TiO_2 Layer on the Photovoltaic Properties of Dye-Sensitized Solar Cells Based on a Co Complex Redox Electrolyte. *Sci. Adv. Mater.* **2016**, *8*, 754–759. [CrossRef]

48. Hu, H.; Shen, J.; Cao, X.; Wang, H.; Lv, H.; Zhang, Y.; Zhu, W.; Zhao, J.; Cui, C. Photo-assisted deposition of Ag nanoparticles on branched TiO_2 nanorod arrays for dye-sensitized solar cells with enhanced efficiency. *J. Alloys Compd.* **2017**, *694*, 653–661. [CrossRef]

49. Feng, P.; Wan, Q.; Wang, T.H. Contact-controlled sensing properties of flowerlike ZnO nanostructures. *Appl. Phys. Lett.* **2005**, *87*, 213111. [CrossRef]